J Supercond Nov Magn (2017) 30:707–714
DOI 10.1007/s10948-016-3886-3

ORIGINAL PAPER

Improvement of the Magnetization of Barium Hexaferrites Induced by Substitution of Nd^{3+} Ions for Fe^{3+} Ions

Wen Chen[1] · Wenwei Wu[1,2] · Minmin Mao[1] · Chong Zhou[1] · Shifang Zhou[1] · Miaoyu Li[1] · Qing Wang[1]

Received: 3 August 2016 / Accepted: 27 October 2016 / Published online: 5 November 2016

Abstract Barium hexagonal ferrites ($BaNd_xFe_{12-x}O_{19}$) have been synthesized by initial high-energy milling of the precursors and calcining subsequently. The as-prepared samples are characterized by X-ray diffraction (XRD), scanning electron microscopy (SEM), and vibrating sample magnetometry (VSM). XRD and SEM examinations reveal that a high-crystallized hexagonal $BaNd_xFe_{12-x}O_{19}$ with lamellar morphology is obtained when the precursor is calcined at 1200 °C in air for 3 h. The hexagonal crystalline structure of $BaFe_{12}O_{19}$ is not changed after doping Nd^{3+} ions in $BaFe_{12}O_{19}$. However, lattice parameters a and b values increase with an increase in Nd content at first, then decrease. Nd substitution may improve the magnetic properties of $BaNd_xFe_{12-x}O_{19}$. $BaNd_{0.1}Fe_{11.9}O_{19}$, obtained at 1050 °C, has the highest specific saturation magnetization value (80.81 emu/g) and magnetic moment (16.21 μ_B); $BaNd_{0.2}Fe_{11.8}O_{19}$, obtained at 950 °C, has the highest coercivity value, 4075.19 Oe.

Keywords Hexagonal ferrites · Chemical synthesis · X-ray diffraction · Magnetic properties

✉ Wenwei Wu
gxuwuwenwei@aliyun.com; wuwenwei@gxu.edu.cn

[1] School of Chemistry and Chemical Engineering, Guangxi University, Nanning 530004, People's Republic of China

[2] Guangxi Colleges and Universities Key Laboratory of Applied Chemistry Technology and Resource Development, Nanning 530004, People's Republic of China

1 Introduction

Ferrimagnetic materials have three types, which are spinel, garnet, and hexaferrites. Among them, synthesis and structural characterization of hexaferrites have received a considerable amount of attention due to the diversity of structure types as well as to their potential applications, such as multiple-state memory elements, novel memory media, transducers, and new functional sensors [1–3]. Hexaferrites are classified into five types, including M, W, Y, X, and Z type hexaferrites with general formulae $BaFe_{12}O_{19}$, $BaMe_2Fe_{16}O_{27}$, $BaMe_2Fe_{12}O_{22}$, $Ba_2Me_2Fe_{28}O_{46}$, and $Ba_2Me_2Fe_{24}O_{41}$, respectively, where Me represents any divalent element [4]. $BaFe_{12}O_{19}$ is one of the M type hexaferrites, which the unit cell contains 38 O^{2-} ions, 2 Ba^{2+} ions, and 24 Fe^{3+} ions. Sixteen Fe^{3+} ions with upward spin are located in three octahedral sites (2a, 12k, and 2b), whereas the remaining eight Fe^{3+} ions with downward spin are at the tetrahedral and trigonal bipyramidal sites ($4f_1$ and $4f_2$) with a net magnetic moment of 40 μ_B per unit cell [5, 6]. The molecular unit of M type hexaferrites is made of one S and one R block, with an overlap of hexagonally and cubically packed layers; the S block consists of two spinel units and the R block consists of three hexagonal units [4]. $BaFe_{12}O_{19}$ is a very important hard magnetic material, which has many unique properties, such as large specific saturation magnetization (Ms) and coercivity (Hc), high values for the magnetic anisotropy field (HA) and Curie temperature, great chemical stability, and excellent high-frequency microwave absorption materials [7, 8]. Substitutions of Fe^{3+} in $BaFe_{12}O_{19}$ with other metal ions lead to net magnetic moment change per unit and tailor magnetic

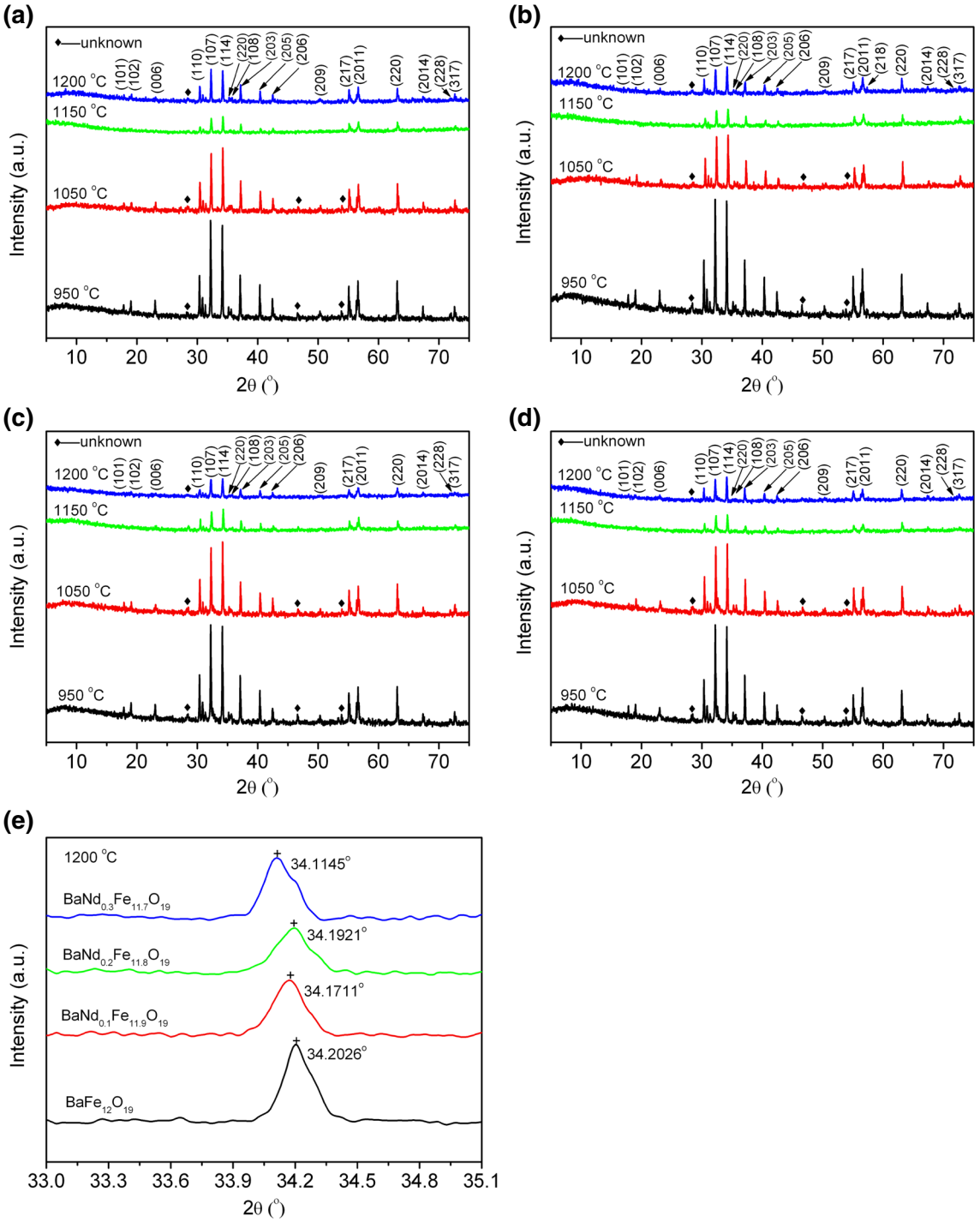

Fig. 1 **a–e** XRD patterns of $BaNd_xFe_{12-x}O_{19}$: **a** $BaFe_{12}O_{19}$, **b** $BaNd_{0.1}Fe_{11.9}O_{19}$, **c** $BaNd_{0.2}Fe_{11.8}O_{19}$, **d** $BaNd_{0.3}Fe_{11.7}O_{19}$, **e** Local magnification

properties of barium hexaferrites. Therefore, doped barium hexaferrites caused great concern.

Various methods of synthesizing $BaFe_{12}O_{19}$ and doped $BaFe_{12}O_{19}$ with different magnetic properties have been developed, including high-energy milling method [9–11], solid-state reaction method [12–14], co-precipitation method [15, 16], hydrothermal treatment [7], sol–gel synthesis [17, 18], citrate precursor [19, 20], self assembly method [21], etc. The magnetic properties of hexaferrite samples depend strongly on composition and synthesis conditions. For example, Venkateswaran et al. [9] synthesized barium hexagonal ferrite ($BaFe_{12}O_{19}$) by initial

high-energy milling of the precursors, followed by sintering at 950 °C in air for 5 h. Specific saturation magnetizations (Ms), remanence (Mr), and coercivity (Hc) of the samples are 45 emu/g, 29 emu/g, and 4500 Oe, respectively. Singh et al. [17] prepared $BaLa_xFe_{12-x}O_{19}$ nanohexaferrites via the sol–gel auto-combustion technique. Specific saturation magnetization of $BaLa_xFe_{12-x}O_{19}$ increases from 72.00 to 78.72 emu/g when doped La content is increased from $x = 0.05$ to $x = 0.25$. Thakur et al. [19] synthesized Sm-doped Ba–Co hexaferrite with composition $BaCo_{0.8}Sm_xFe_{(11.2-x)}O_{19}$ ($x = 0.2$, 0.4, and 0.6) via a citrate precursor method. The $BaCo_{0.8}Sm_{0.2}Fe_{11}O_{19}$ sample, sintered at 900 °C, has the highest specific saturation magnetization (32.55 emu/g) and the highest coercivity (2690.20 Oe) value. However, to the best of our knowledge, the synthesis and magnetic properties of $BaNd_xFe_{12-x}O_{19}$ by thermal decomposition of oxalates have not been reported in previous studies.

This study aims to prepare $BaNd_xFe_{12-x}O_{19}$ by calcining oxalates in air and study the effect of composition and calcination temperature on magnetic properties of $BaNd_xFe_{12-x}O_{19}$. Our results clearly show that the magnetic properties, in particular the specific magnetizations (Ms) and coercivity (Hc) of $BaNd_xFe_{12-x}O_{19}$, can be improved after doping Nd^{3+} ions.

2 Experimental Procedures

All chemicals used are of reagent-grade purity (purity >99.9 %). The $BaNd_xFe_{12-x}O_{19}$ was prepared by initial planetary ball milling of the precursors and calcining subsequently. In a typical synthesis ($BaFe_{12}O_{19}$), 1.18 g $BaC_2O_4 \cdot 2H_2O$, 9.71 g $FeC_2O \cdot 2H_2O$, and 10 ml ethanol were added to a stainless steel ball milling tank of 100 ml. The mass ratio of the sample to the stainless steel ball is about 1/15. Samples were milled at room temperature for 30 min. The grinding velocity was about 350 circles/min. $BaFe_{12}O_{19}$ precursor was obtained after being dried at 80 °C in air for 5 h. A similar synthesis procedure was used to synthesize other $BaNd_xFe_{12-x}O_{19}$ precursor. Finally, the $BaNd_xFe_{12-x}O_{19}$ precursor was calcined over 950 °C for 3 h at a heating rate of 2 °C min^{-1} in air to produce hexagonal $BaNd_xFe_{12-x}O_{19}$.

X-ray diffraction (XRD) of the prepared sample was carried out using an X/pert PRO diffractometer equipped with a graphite monochromator and a Cu target. Radiation applied was Cu Kα ($\lambda = 0.15406$ nm), operating at 40 kV and 50 mA. XRD scans were conducted from 5 to 75° in 2θ, with a step size of 0.01°. The morphologies of the synthesis products were observed using a S-3400 scanning electron microscope (SEM). The magnetic properties of the samples were studied by vibrating sample magnetometer (VSM, Lake Shore 7410) at room temperature (RT).

3 Results and Discussion

3.1 XRD and SEM Analyses of the Calcined Products

Figure 1 shows XRD patterns of $BaNd_xFe_{12-x}O_{19}$ calcined at different temperatures for 3 h. Characteristic diffraction peaks of hexagonal $BaFe_{12}O_{19}$ and an unknown phase appeared when $BaNd_xFe_{12-x}O_{19}$ precursors were calcined at 950 °C. Characteristic diffraction peaks of the unknown phase become weak and/or disappeared with the increase in calcination temperature. When $BaNd_xFe_{12-x}O_{19}$ precursors were calcined at 1200 °C for 3 h, all diffraction peaks in the pattern were in accord with those of hexagonal $BaFe_{12}O_{19}$ with space group P63/mmc(194) from PDF card 43-0002 except for a weak diffraction peak at 28.39° for 2θ. The Nd^{3+}-doped ions do not change the hexagonal crystalline structure of $BaFe_{12}O_{19}$ except that the diffraction peaks slightly shift (Fig. 1e). The lattice parameters of the sample were refined by the Rietveld analysis using MDI Jade (ver. 5.0) software. The refined lattice parameters of $BaNd_xFe_{12-x}O_{19}$, obtained at 1200 °C, are shown in Table 1. With increase in Nd doping from $x = 0$, 0.1, 0.2, to 0.3, lattice parameters (a and b values) increase at first, then decrease; the c value decreases at first, then increases. This could be due to the larger Nd^{3+} ion (0.099 nm) [22] substituting the Fe^{3+} ion in a and b axes (with a much smaller ionic radius of 0.067 nm) [23] initially, and then for a higher doping level ($x = 0.3$), some of the Ba^{2+} ions (0.161 nm) [24] could enter the c axis.

The crystallite size of $BaNd_xFe_{12-x}O_{19}$ is estimated using the following Scherrer formula [25]:

$$D = K\lambda/(\beta\cos\theta) \quad (1)$$

where D is the crystallite size, $K = 0.89$ (the Scherrer constant), $\lambda = 0.15406$ nm (wavelength of the X-ray used), β is the width at half-maximum intensity, and θ is

Table 1 The lattice parameters of $BaNd_xFe_{12-x}O_{19}$ ($x = 0.0$, 0.1, 0.2, and 0.3)

Nd content, x	a (nm)	b (nm)	c (nm)
0.0	0.58919(9)	0.58919(9)	2.31831(7)
0.1	0.58921(1)	0.58921(1)	2.31826 (2)
0.2	0.58921(1)	0.58921(1)	2.31823(0)
0.3	0.58920(0)	0.58920(0)	2.31830(4)

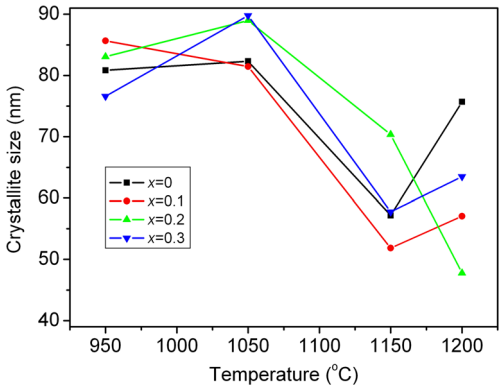

Fig. 2 Dependence of crystallite size of $BaNd_xFe_{12-x}O_{19}$ on calcination temperature

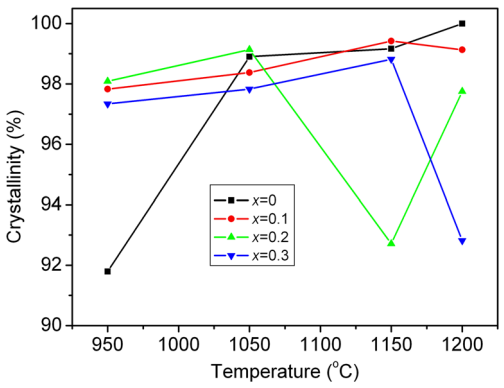

Fig. 4 Dependence of crystallinity of $BaNd_xFe_{12-x}O_{19}$ on calcination temperature and Nd content

the corresponding angle. The $d_{(114)}$ interplanar spacing of $BaNd_xFe_{12-x}O_{19}$ is determined using the Bragg equation [25]:

$$d_{(114)} = \frac{\lambda}{2\sin\theta_{(114)}}, \tag{2}$$

The crystallite size (D) of $BaNd_xFe_{12-x}O_{19}$, obtained at different temperatures, and $d_{(114)}$ interplanar spacing of $BaNd_xFe_{12-x}O_{19}$, obtained at 1200 °C, are shown in Figs. 2 and 3, respectively From Fig. 2, the crystallite size of $BaNd_xFe_{12-x}O_{19}$, obtained at 1200 °C, exhibits nonlinear variation; the crystallite size of $BaNd_xFe_{12-x}O_{19}$ is between 47.8 and 75.7 nm. By contrast, $d_{(114)}$ interplanar spacing of $BaNd_xFe_{12-x}O_{19}$ decreases with the increase in Nd content (Fig. 3).

The crystallinity of $BaNd_xFe_{12-x}O_{19}$ can be estimated by MDI Jade 5.0 software. The crystallinity of $BaNd_xFe_{12-x}O_{19}$ ($x = 0, 0.1, 0.2$, and 0.3), obtained at different temperatures, is shown in Fig. 4. The crystallinities of $BaNd_xFe_{12-x}O_{19}$, obtained at 1200 °C, decrease with increase in Nd content.

Lattice strains of the $BaNd_xFe_{12-x}O_{19}$ are determined using the following Williamson–Hall formula [25]:

$$\varepsilon = \frac{\beta}{4\tan\theta}, \tag{3}$$

where β is the full-width at half maximum (in radian) of the peaks, θ is the peak position, and ε is the lattice strain of the structure. Lattice strains of $BaNd_xFe_{12-x}O_{19}$, obtained at 1200 °C, are shown in Fig. 5. The lattice strain of $BaNd_xFe_{12-x}O_{19}$ increases with an increase in Nd content ($0 \le x \le 0.2$) at first and then decreases ($x = 0.3$). The lattice strain exists in the $BaFe_{12}O_{19}$, attributed that Ba^{2+} (0.161 nm) [24] and Fe^{2+} (0.067 nm) [23] ions have different ionic radii and/or charge, resulting in the distortion of octahedral, tetrahedral, and trigonal bipyramidal. The substitution of Fe^{3+} ions in a and b axes of the hexagonal by Nd^{3+} ions with larger ionic radii can increase the distortion of hexagonal in $BaNd_xFe_{12-x}O_{19}$, resulting in the increase of lattice strain in $BaNd_xFe_{12-x}O_{19}$ with increasing Nd content. However, for a higher doping level ($x = 0.3$), the replacement of some Fe^{3+} ions in the c axis by Nd^{3+} ions decreases the distortion in $BaNd_xFe_{12-x}O_{19}$, resulting in the decrease of lattice strain.

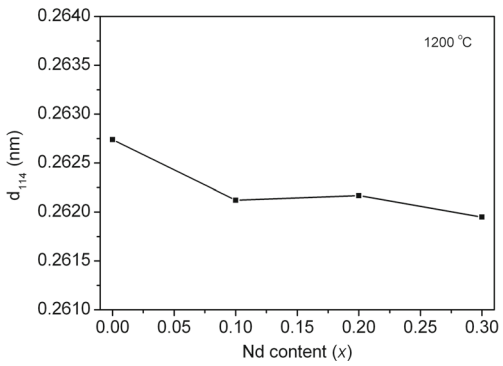

Fig. 3 Dependence of interplanar spacing (d_{114}) of $BaNd_xFe_{12-x}O_{19}$ on Nd content

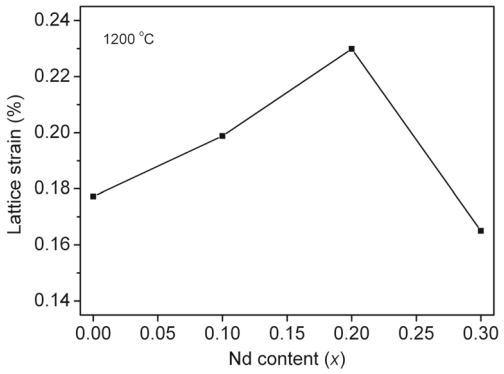

Fig. 5 Dependence of lattice strain of $BaNd_xFe_{12-x}O_{19}$ on Nd content

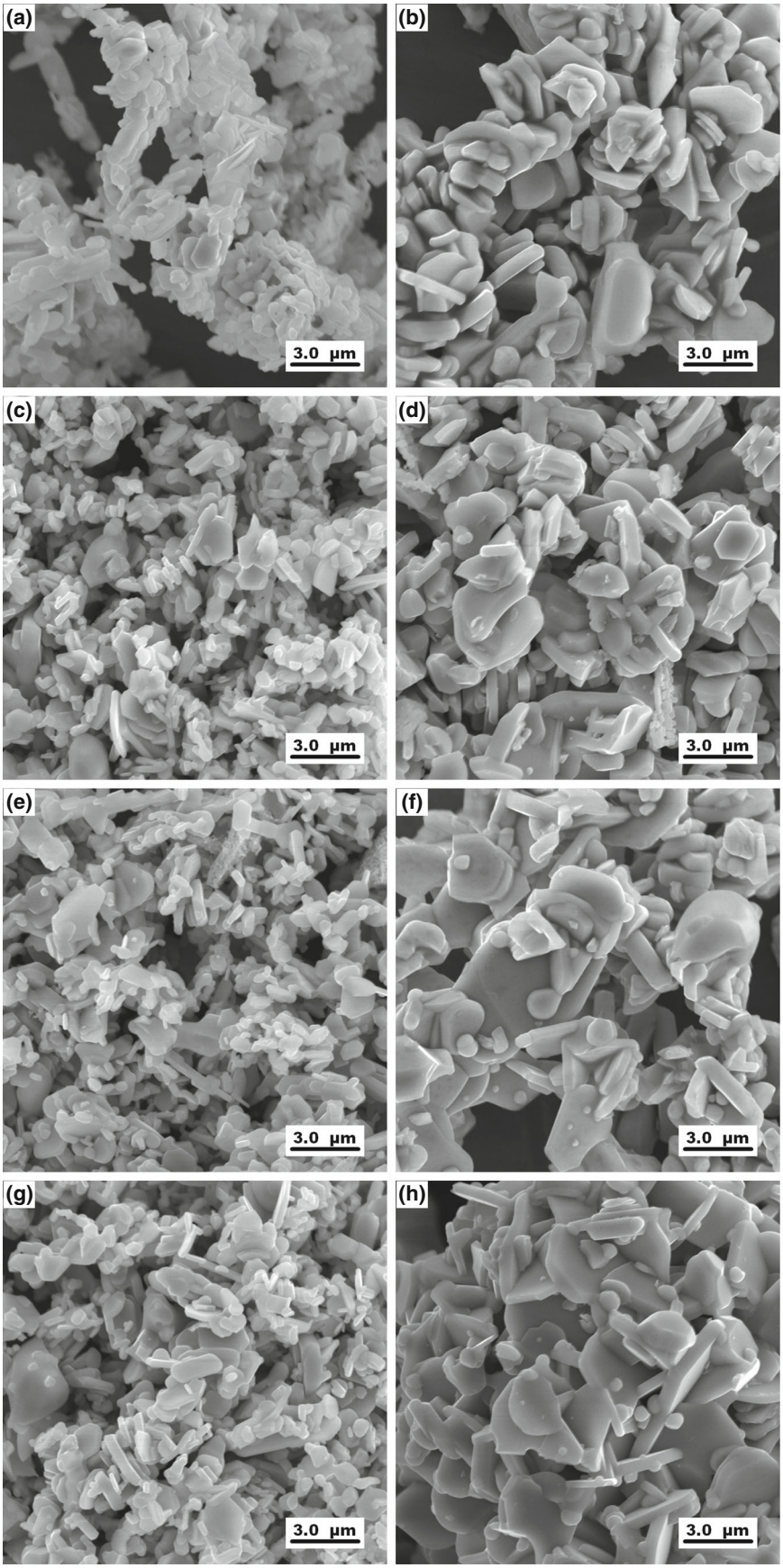

Fig. 6 SEM images of $BaNd_xFe_{12-x}O_{19}$: $BaFe_{12}O_{19}$ (**a** 1050 °C, **b** 1200 °C), $BaNd_{0.1}Fe_{11.9}O_{19}$ (**c** 1050 °C, **d** 1200 °C), $BaNd_{0.2}Fe_{11.8}O_{19}$ (**e** 1050 °C, **f** 1200 °C), and $BaNd_{0.3}Fe_{11.7}O_{19}$ (**g** 1050 °C, **h** 1200 °C)

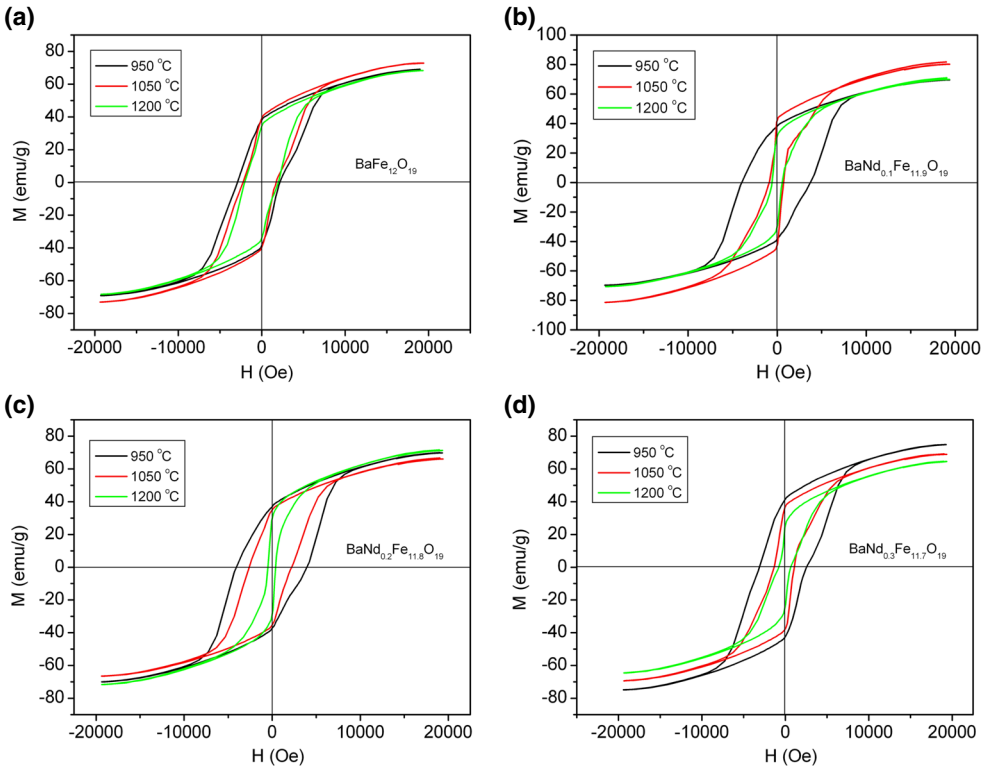

Fig. 7 **a–d** M–H (magnetization–hysteresis) loops of $BaNd_xFe_{12-x}O_{19}$ samples obtained at different temperatures in air for 3 h

The morphologies of the calcined products are shown in Fig. 6. $BaNd_xFe_{12-x}O_{19}$ ($x = 0, 0.1, 0.2$, and 0.3) samples, obtained at 1050 and 1200 °C, are composed of approximately lamellar grains. The particle size increases with an increase of calcination temperature. The particle size of $BaNd_xFe_{12-x}O_{19}$, obtained at 1200 °C, is mainly between 500 nm and 3 μ m.

3.2 Magnetic Properties of $BaNd_xFe_{12-x}O_{19}$

Figure 7 shows RT magnetic hysteresis loops of the as-prepared $BaNd_xFe_{12-x}O_{19}$ samples. Effects of Nd content and calcination temperature on specific magnetization are presented in Fig. 8. Dependence of specific saturation magnetizations of $BaNd_xFe_{12-x}O_{19}$ on Nd content exhibits non-linear variation. $BaNd_{0.1}Fe_{11.9}O_{19}$, obtained at 1050 °C, has the highest specific saturation magnetization value (80.81 emu/g); $BaNd_{0.3}Fe_{11.7}O_{19}$, obtained at 1200 °C, has the lowest specific saturation magnetization value (64.22 emu/g). The evolution of specific saturation magnetization of $BaNd_xFe_{12-x}O_{19}$, obtained at 1200 °C, can be explained as follows: The magnetic moments per ion for Ba^{2+}, Nd^{3+}, and Fe^{3+} ions are 0, 3, and 5 μ_B, respectively. When Fe^{3+} ions in hexagonal $BaFe_{12}O_{19}$ are partially substituted by Nd^{3+} ions, Nd^{3+} ions preferentially fill the tetrahedral and trigonal bipyramidal sites, resulting in the increase in the net magnetic moment and/or specific saturation magnetization of $BaNd_xFe_{12-x}O_{19}$ with the increase of Nd content initially, and then for a higher doping level ($x = 0.3$), some of the Nd^{3+} could enter the octahedral sites, resulting in the decrease of the net magnetic moment and/or specific saturation magnetization of $BaNd_xFe_{12-x}O_{19}$.

Dependence of remanence (Mr) and coercivity (Hc) on Nd content and calcination temperature is shown in Fig. 9. From Fig. 9a, remanences of $BaNd_xFe_{12-x}O_{19}$ decrease with an increase in calcination temperature except for 950 °C; that of $BaNd_xFe_{12-x}O_{19}$, obtained at 1200 °C, decreases with an increase in Nd content. By contrast, coercivity of $BaNd_xFe_{12-x}O_{19}$ decreases with an increase in

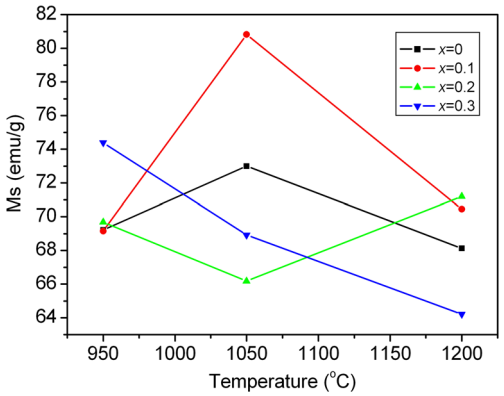

Fig. 8 Dependence of specific saturation magnetization of $BaNd_xFe_{12-x}O_{19}$ on Nd content and calcination temperature

calcination temperature (Fig. 9b). Dependence of coercivity of $BaNd_xFe_{12-x}O_{19}$ on Nd content exhibits non-linear variation. $BaNd_{0.2}Fe_{11.8}O_{19}$, obtained at 950 °C, has the highest coercivity value (4075.19 Oe); $BaNd_{0.2}Fe_{11.8}O_{19}$, obtained at 1200 °C, has the lowest coercivity value (481.2 Oe). Dependence of squareness (Mr/Ms) on Nd content is shown in Fig. 10a. Squareness (Mr/Ms) of $BaNd_xFe_{12-x}O_{19}$ decreases with an increase of calcination temperature; that of $BaNd_xFe_{12-x}O_{19}$, obtained at 1200 °C, decreases with an increase in Nd content. $BaNd_{0.3}Fe_{11.7}O_{19}$ has the lowest Mr/Ms, 0.3625.

The magnetic moment of $BaNd_xFe_{12-x}O_{19}$ samples obtained at 1200 °C is estimated using the following formula [26]:

$$\eta_B = M \times Ms/5585, \quad (4)$$

where M is the molecular weight of the composition, Ms is the specific saturation magnetization (emu/g), and η_B is the magnetic moment (μ_B). The results show that dependence

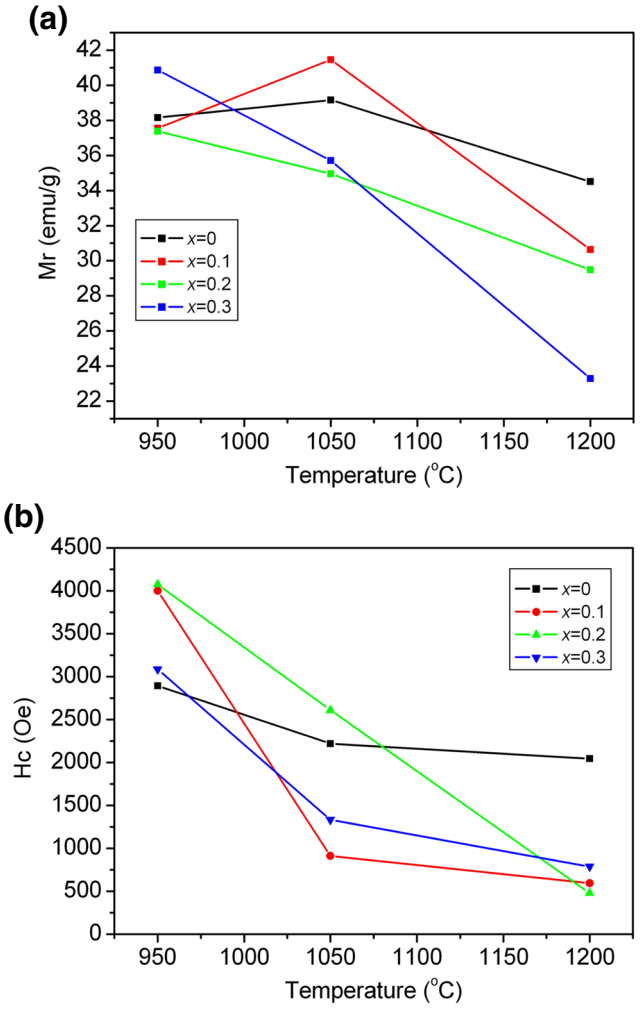

Fig. 9 **a**, **b** Dependence of remanence (Mr) and coercivity (Hc) of $BaNd_xFe_{12-x}O_{19}$ on Nd content and calcination temperature

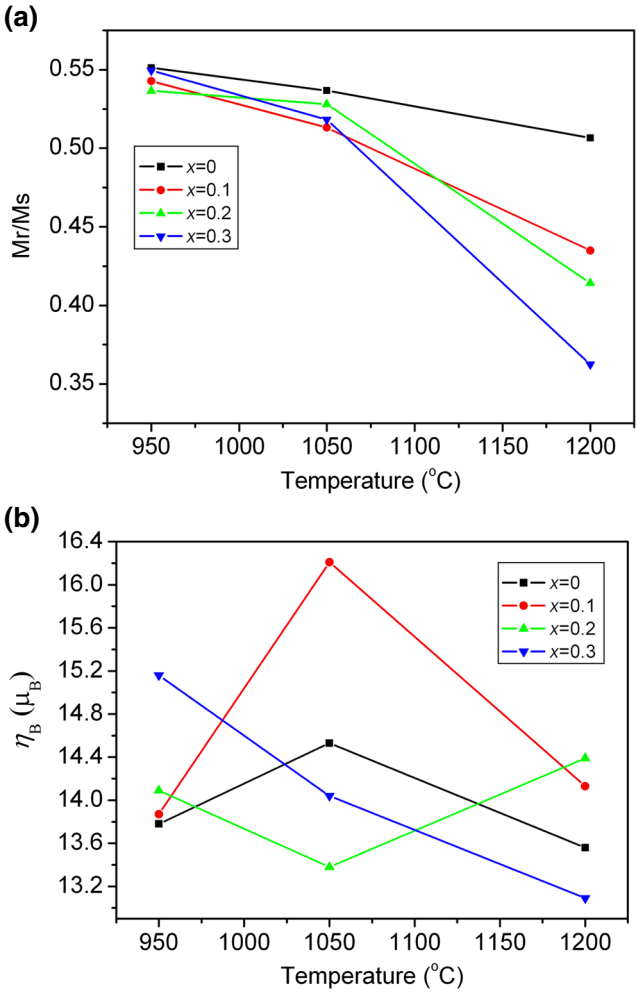

Fig. 10 **a**, **b** Dependence of squareness (Mr/Ms) and magnetic moment (η_B) of $BaNd_xFe_{12-x}O_{19}$ on Nd content and calcination temperature

of the magnetic moment of $BaNd_xFe_{12-x}O_{19}$ on Nd content exhibits non-linear variation (Fig. 10b). $BaNd_{0.1}Fe_{11.9}O_{19}$, obtained at 1050 °C, has the largest magnetic moment value (16.21 μ_B); $BaNd_{0.3}Fe_{11.7}O_{19}$, obtained at 1200 °C, has the lowest magnetic moment value (13.09 μ_B).

4 Conclusions

Barium hexagonal ferrites ($BaNd_xFe_{12-x}O_{19}$) have been successfully synthesized by ball milling a mixture of oxalates at first, followed by calcination in air. XRD and SEM examinations indicate that a high-crystallized hexagonal $BaNd_xFe_{12-x}O_{19}$ with lamellar morphology is obtained when the precursor is calcined above 950 °C in air for 3 h. The hexagonal crystalline structure of $BaFe_{12}O_{19}$ is not changed after doping Nd^{3+} ions in $BaFe_{12}O_{19}$. However, lattice parameters a and b values increase at first, then

decrease; the c value decreases at first, then increases. The lattice strain of $BaNd_xFe_{12-x}O_{19}$ increases with an increase in Nd content ($0 \leq x \leq 0.2$) at first and then decreases ($x = 0.3$). Specific saturation magnetization and the magnetic moment of $BaNd_xFe_{12-x}O_{19}$ exhibit non-linear variation. Nd substitution may improve magnetic properties of $BaNd_xFe_{12-x}O_{19}$. $BaNd_{0.1}Fe_{11.9}O_{19}$, obtained at 1050 °C, has the highest specific saturation magnetization value (80.81 emu/g) and magnetic moment (16.21 μ_B); $BaNd_{0.2}Fe_{11.8}O_{19}$, obtained at 950 °C, has the highest coercivity value, 4075.19 Oe.

Acknowledgments This study was financially supported by the National Natural Science Foundation of China (Grant no. 21161002, 21603040), the Guangxi Natural Science Foundation of China (Grant no. 2016GXNSFDA380034, 2016GXNSFBA380062), and the Guangxi University Student Innovation Foundation of China (Grant no. 30).

References

1. Tawfik, A., Hemeda, O.M., El-Sayed, A.H., Hamad, M.A.: J. Supercond. Nov. Magn. **29**, 2085–2088 (2016)
2. Jaafar, A., Almisaeed, A., Souier, T., Bououdina, M.: J. Supercond. Nov. Magn. (2016). doi:10.1007/s10948-016-3593-0
3. Torkian, S., Ghasemi, A., ShojaRazavi, R., Tavoosi, M.: J. Supercond. Nov. Magn. **29**, 1627–1640 (2016)
4. Pawar, R.A., Desai, S.S., Tamboli, Q.Y., Shirsath, S.E., Patange, S.M.: J. Magn. Magn. Mater. **378**, 59–63 (2015)
5. Verma, S., Pandey Jr., O.P., A.P., Sharma, P.: Physica B **448**, 57–59 (2014)
6. Wu, C.J., Yu, Z., Yang, Y., Sun, K., Nie, J.L., Liu, Y., Jiang, X.N., Lan, Z.W.: J. Alloy. Compd. **664**, 406–410 (2016)
7. Wang, J., Wu, Y.J., Zhu, Y.J., Wang, P.Q.: Mater. Lett. **61**, 1522–1525 (2007)
8. Mohsen, Q.: J. Alloy. Compd. **500**, 125–128 (2010)
9. Manikandan, M., Venkateswaran, C.: J. Magn. Magn. Mater., 82–86 (2014). 358–359
10. Shams, M.H., Rozatian, A.S.H., Yousefi, M.H., Valíček, J., Šepelák, V.: J. Magn. Magn. Mater. **399**, 10–18 (2016)
11. Kaynar, M.B., Özcana, Ş., Shah, S.I.: Ceram. Int. **41**, 11257–11263 (2015)
12. Trukhanov, A.V., Turchenko, V.O., Bobrikov, I.A., Trukhanov, S.V., Kazakevich, I.S., Balagurov, A.M.: J. Magn. Magn. Mater. **393**, 253–259 (2015)
13. El-Sayed, S.M., Meaz, T.M., Amer, M.A., El Shersaby, H.A.: Physica B **426**, 137–143 (2013)
14. Yang, H.B., Liu, M., Lin, Y., Dong, G.Q., Hu, L.Y., Zhang, Y., Tan, J.Y.: Mater. Chem. Phys. **160**, 5–11 (2015)
15. Mosleh, Z., Kameli, P., Ranjbar, M., Salamati, H.: Ceram. Int. **40**, 7279–7284 (2014)
16. Amer, M.A., Meaz, T.M., Attalah, S.S., Ghoneim, A.I.: Mater. Sci. Semicond. Process. **40**, 374–382 (2015)
17. Pratap Singh, V., Kumar, G., Kumar, A., Rai, R.S., Valente, M.A., Batoo, K.M., Kotnala, R.K., Singh, M.: Ceram. Int. **42**, 5011–5017 (2016)
18. Chavan, V.C., Shirsath, S.E., Mane, M.L., Kadam, R.H., More, S.S.: J. Magn. Magn. Mater. **398**, 32–37 (2016)
19. Rana, K., Thakur, P., Thakur, A., Tomar, M., Gupta, V., Mattei, J.L., Queffelec, P.: Ceram. Int. **42**, 8413–8418 (2016)
20. Ahmed, M.A., Mansour, S.F., Ismael, H.: J. Magn. Magn. Mater. **378**, 376–388 (2015)
21. Choi, M., Cho, S., Song, Y., Baek, S., Kim, H., Jung, J., Lee, H., Park, C., Park, S., kim, Y.: Curr. Appl. Phys. **14**, 1208–1211 (2014)
22. Yildirim, S., Yurddaskal, M., Dikici, T., Aritman, I., Ertekin, K., Celik, E.: Ceram. Int. **42**, 10579–10586 (2016)
23. Huang, X.S., Zhou, Y., Wu, W.W., Xu, J.W., Liu, S.Q., Liu, D.S., Wu, J.: J. Electron. Mater. **45**, 3113–3120 (2016)
24. Manoun, B., Ezzahi, A., Benmokhtar, S., Ider, A., Lazor, P., Bihd, L., Igartua, J.M.: J. Alloy. Compd. **533**, 43–52 (2012)
25. Huang, X.S., Chen, W., Wu, W.W., Zhou, Y., Wu, J., Wang, Q., Chen, Y.Y.: J. Mater. Sci. - Mater. Electron. **27**, 5395–5402 (2016)
26. Chen, W., Zhou, Y., Lu, J.Y., Huang, X.S., Wu, W.W., Lin, C.W., Wang, Q.: Ceram. Int. **42**, 1114–1121 (2016)